

## Article

# Improvement of Piezoelectricity of $(\text{Bi}_{0.5}\text{Na}_{0.5})_{0.94}\text{Ba}_{0.06}\text{TiO}_3$ Ceramics Modified by a Combination of Porosity and $\text{Sm}^{3+}$ Doping

Siyu Xia, Huiling Du , Zhuo Li, Fan Zhao, Qianqian Li, Yuxuan Hu and Le Kang

College of Materials Science and Engineering, Xi'an University of Science and Technology, Xi'an 710054, China; 20211225040@stu.xust.edu.cn (S.X.); 21120089015@stu.xust.edu.cn (Z.L.); 21211225041@stu.xust.edu.cn (F.Z.); 21211025017@stu.xust.edu.cn (Q.L.); 21211225053@stu.xust.edu.cn (Y.H.); kangle20140805@126.com (L.K.)

\* Correspondence: hldu@xust.edu.cn

**Abstract:** Porous lead-free piezoelectric ceramics are characterized by their environment-friendly, light weight, and large specific surface area. The optimization of porous  $\text{Na}_{0.5}\text{Bi}_{0.5}\text{TiO}_3$ -based lead-free piezoelectric ceramics can improve piezoelectric properties, enhance force–electric coupling characteristics, and effectively promote energy conversion, expanding the application in force–electric coupling devices. This study aimed to prepare  $[\text{Sm}_x(\text{Bi}_{0.5}\text{Na}_{0.5})_{1-3x/2}]_{0.94}\text{Ba}_{0.06}\text{TiO}_3$  ( $x = 0, 0.01, 0.02, 0.03, 0.04$ ) lead-free ceramics with porous structures, resulting in the piezoelectric constant  $d_{33} = 131$  pC/N and the plane electromechanical coupling coefficient  $k_p = 0.213$  at  $x = 0.01$ . The presence of pores in lead-free ceramics has a direct impact on the domain structure and can cause the depolarization process to relax. Then, the soft doping of  $\text{Sm}^{3+}$  makes the A-site ion in porous  $(\text{Bi}_{0.5}\text{Na}_{0.5})_{0.94}\text{Ba}_{0.06}\text{TiO}_3$  ceramics occupancy inhomogeneous and generates cation vacancies, which induces lattice distortion and makes the domain wall motion easier, resulting in the improvement of piezoelectric properties and electromechanical coupling parameters. Furthermore, the piezoelectric oscillator exhibits greater resistance to resonant coupling in the radial extension vibration mode. These results infer that a combination of porosity and  $\text{Sm}^{3+}$  doping renders  $(\text{Bi}_{0.5}\text{Na}_{0.5})_{0.94}\text{Ba}_{0.06}\text{TiO}_3$  ceramics base material for piezoelectric resonators, providing a scientific basis for their application in force–electric coupling devices, such as piezoelectric resonant gas sensors.

**Keywords:**  $(\text{Bi}_{0.5}\text{Na}_{0.5})_{0.94}\text{Ba}_{0.06}\text{TiO}_3$ ; porous ceramics;  $\text{Sm}^{3+}$  doping; piezoelectric properties



**Citation:** Xia, S.; Du, H.; Li, Z.; Zhao, F.; Li, Q.; Hu, Y.; Kang, L. Improvement of Piezoelectricity of  $(\text{Bi}_{0.5}\text{Na}_{0.5})_{0.94}\text{Ba}_{0.06}\text{TiO}_3$  Ceramics Modified by a Combination of Porosity and  $\text{Sm}^{3+}$  Doping. *Coatings* **2023**, *13*, 805. <https://doi.org/10.3390/coatings13040805>

Academic Editor: Günter Motz

Received: 17 March 2023

Revised: 7 April 2023

Accepted: 18 April 2023

Published: 21 April 2023



**Copyright:** © 2023 by the authors. Licensee MDPI, Basel, Switzerland. This article is an open access article distributed under the terms and conditions of the Creative Commons Attribution (CC BY) license (<https://creativecommons.org/licenses/by/4.0/>).

## 1. Introduction

As electronic information technology continues to evolve with increasing integration, miniaturization, and intelligence [1–3], electronic ceramics have emerged as a critical technology that impacts its development. Currently, research efforts are primarily focused on piezoelectric ceramics based on lead zirconate titanate (PZT). However, the lead element contained in lead-based piezoelectric ceramics is harmful to human health and the environment and is highly restricted in practical applications [4–6]. Consequently, many researchers face the significant challenge of developing multifunctional lead-free ceramics that can be used in a range of applications.

$\text{Na}_{0.5}\text{Bi}_{0.5}\text{TiO}_3$  (NBT)-based ceramics are a type of perovskite-based, lead-free piezoelectric material with a high Curie temperature, large stress–strain capabilities, and excellent piezoelectric properties. As such, these materials have been employed in a broad range of applications, such as sensors, brakes, and transducer ultrasonic motors [7–11]. In recent years, NBT has been modified to form a morphotropic phase boundary (MPB) with other  $\text{ABO}_3$  perovskite compositions, such as  $(1 - x)\text{Bi}_{0.5}\text{Na}_{0.5}\text{TiO}_3 - x\text{BaTiO}_3$  [12–15]. Through such research, it has been discovered that the optimal composition is achieved at  $x = 0.06$  ( $(\text{Bi}_{0.5}\text{Na}_{0.5})_{0.94}\text{Ba}_{0.06}\text{TiO}_3$ ) [16]. Nevertheless, in practical applications, the use of dense

ceramics as excitation materials in hydroacoustic transducers is limited by their high dielectric constant and density. Therefore, research on the integration of the structure and function of porous piezoelectric ceramics has garnered significant attention [17–20].

The high porosity of porous ceramics can simplify the piezoelectric resonance characteristics and promote effective energy conversion, making them suitable for use in force-coupled devices [21–25]. However, porous ceramics with high porosity can significantly reduce their piezoelectric properties, making them susceptible to external interference in practical applications. Therefore, improving sensitivity and resistance to external interference while maintaining a complex pore structure is a key research area.

Currently, ion doping is a popular method for enhancing the piezoelectric characteristics of lead-free ceramics [26,27]. Hao et al. [28] introduced rare earth oxides, such as  $\text{Pr}_2\text{O}_3$ ,  $\text{Eu}_2\text{O}_3$ , and  $\text{Sm}_2\text{O}_3$ , to  $(1-x)[(0.93(\text{Na}_{0.5}\text{Bi}_{0.5})\text{TiO}_3-0.07\text{BaTiO}_3)]-x\text{RE}$  ceramics. This modulation of the components led to  $d_{33}$  values of 163 pC/N, 175 pC/N, and 213 pC/N, respectively, with corresponding strains of 0.13%, 0.14%, and 0.17%. In another study, Kong et al. [29] reported that the doping of Mn to  $0.94(\text{Bi}_{0.5}\text{Na}_{0.5})\text{TiO}_3-0.06\text{BaTiO}_3$  resulted in a high  $d_{33}$  of 166 pC/N and a large strain of 0.30%, thus combining existing research based on the simplified piezoelectric resonance of porous structures and then improving the adverse effects of porous structures on the piezoelectric properties of ceramics through doping. Soft doping as a means of doping is also known as sender doping. It is a doping method in which low-valent positive ions are replaced by high-valent positive ions. According to the requirement of electrical neutrality, cation vacancies will appear in the sample and the domain walls will move easily under the action of electric fields or external forces, thus softening the material properties. This means of ion doping can be used not only for the modulation of dense ceramic systems but also for the property modulation of porous ceramics.  $\text{Sm}^{3+}$  has a very similar ionic radius to the A-site ions ( $\text{Bi}^{3+}$ ,  $\text{Na}^+$ ) of  $(\text{Bi}_{0.5}\text{Na}_{0.5})_{0.94}\text{Ba}_{0.06}\text{TiO}_3$  (BNBT6) ceramics compared with other rare earth elements [30], so it can more easily access BNBT6 ceramics and affect their piezoelectric properties. However, currently, there are no published studies on the enhancement of the properties of porous BNBT6 ceramics through  $\text{Sm}_2\text{O}_3$  doping.

This study focuses on the preparation of porous  $[\text{Sm}_x(\text{Bi}_{0.5}\text{Na}_{0.5})_{1-3x/2}]_{0.94}\text{Ba}_{0.06}\text{TiO}_3$  (BNBT6- $x\text{Sm}$ ) ceramics and investigates the influence of  $\text{Sm}^{3+}$  soft doping on the dielectric properties, piezoelectric properties, and resonance characteristics of BNBT6 ceramics. The findings suggest that the combination of pore and  $\text{Sm}^{3+}$  doping improves the piezoelectric properties and resonance characteristics of porous BNBT6 ceramics, providing valuable insights for future research and application in this field.

## 2. Experimental

$\text{Na}_{0.5}\text{Bi}_{0.5}\text{TiO}_3$  (NBT) is made of  $\text{TiO}_2$  (>99.9%, Macklin),  $\text{Bi}_2\text{O}_3$  (>99.9%, Macklin), and  $\text{Na}_2\text{CO}_3$  (>99.9%, Macklin), ball milled at 350 r/min for 8 h according to a certain recipe, then dried at 60 °C and pre-sintered at 800 °C and held for 2 h to obtain NBT ceramic powder. The ceramic powder was put into the ball mill jar for 12 h of secondary ball milling to obtain a powder with finer particle size and uniform distribution.

$[\text{Sm}_x(\text{Bi}_{0.5}\text{Na}_{0.5})_{1-3/2x}]_{0.94}\text{Ba}_{0.06}\text{TiO}_3$  powders ( $x = 0, 0.01, 0.02, 0.03, 0.04$ ), referred to as BNBT6- $x\text{Sm}$ , were prepared via the solid-state reaction using  $\text{Na}_2\text{CO}_3$  (>99.8%, Macklin),  $\text{Bi}_2\text{O}_3$  (>99.9%, Macklin),  $\text{TiO}_2$  (>99.9%, Macklin),  $\text{BaCO}_3$  (>99.9%, Macklin), and  $\text{Sm}_2\text{O}_3$  (>99.9%, Macklin) as base materials. The raw materials were weighed based on the stoichiometric ratio and then ball milled for 8 h at 350 r/min with zirconia balls in a 20 mL nylon bottle with ethanol. The resulting solution was dried for 12 h and then calcined at 870 °C for 3 h. Then calcined powders were re-milled for 6 h to break up any agglomerates. The pre-synthesized BNBT6- $x\text{Sm}$  powders were then obtained by passing them through a 100-mesh sieve after drying.

Porous BNBT6- $x\text{Sm}$  ceramic powder was prepared by mixing self-made BNBT6 ceramic powder with 10 wt.% kiwi pollen (Baoji, Shaanxi Province) using the dry-mixing method. Then, 0.3 g BNBT6- $x\text{Sm}$  powder was weighed and subjected to cold isostatic

pressure at 150 Mpa to obtain the ceramic billet with a diameter of 10 mm. The sample was first heated at 3 °C/min to 550 °C for 2 h to completely burn the pollen template and eliminate the gas, thus forming the template pores. The sample was heated to 800 °C at 5 °C/min in the high-temperature chamber furnace (KSL-1500XS), then slowly heated to 1150 °C at 3 °C/min and held for 2 h, and then cooled to room temperature at 5 °C/min. Finally, silver was deposited onto the surface of the ceramic and heated at 800 °C for 15 min at a heating rate of 5 °C/min. Silver as the electrode does not cause secondary effects.

The phase structure of the samples was analyzed by X-ray diffraction (XRD; D8 Advance, Brook AXS, Karlsruhe, Germany), with a scanning rate of 10°/min in the range of 20°–80°. The microstructures were observed using scanning electron microscopy (SEM; SU3500, Hitachi, Tokyo, Japan), with a voltage of 20 kV. The dielectric constant and dielectric loss of the samples were measured using a precision impedance analyzer (E4980A, Agilent, Santa Clara, CA, USA) connected to a temperature controller (Gjw-1) at 25–450 °C with the frequency of 1 kHz–1000 kHz. The hysteresis loop and strain curve were measured using a ferroelectric analyzer (TF 2000, aixACCT, Aachen, Germany) at 10 Hz. The  $d_{33}$  of all porous ceramic samples was measured at 110 Hz using the DZ-2671A pressure tester and ZJ-5A quasi-static piezoelectric constant tester. The impedance spectrum/impedance angular spectrum ( $Z/\theta$ ) at 0–1 MHz of the sample was measured by using the measurement and control communication software based on GPIB communication protocol and Agilent4980E automatic balance digital bridge. The resonant frequency ( $f_r$ ) and anti-resonant frequency ( $f_a$ ) of the porous ceramics were obtained.

### 3. Results and Discussion

#### 3.1. Phase Structures and Morphologies of the Porous BNBT6-*x*Sm Ceramics

The XRD patterns for NBT and BNBT6 ceramic powders are presented in Figure 1a, where both powders exhibit a perovskite phase structure with no secondary phases detected. The preparation of BNBT6 ceramics with a perovskite phase was achieved through the solid-phase reaction, and this powder is able to serve as a fundamental component for the fabrication of porous BNBT6 ceramics.

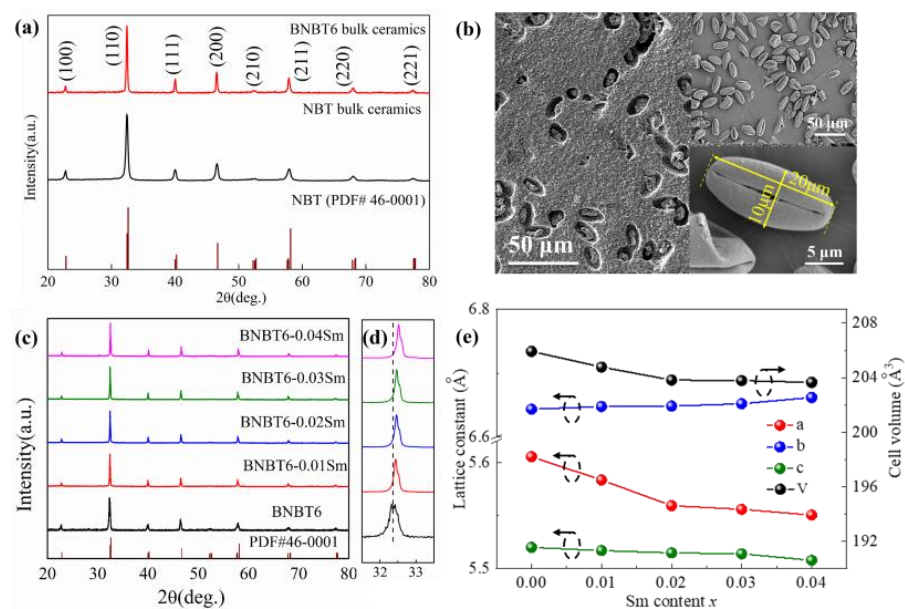


**Figure 1.** (a) XRD patterns of NBT and BNBT6 ceramics at 20°–80°. (b) SEM image of porous BNBT6 ceramic with 10 wt.% pollen, and the embedded graph is the SEM image of kiwi pollen. (c) XRD patterns of porous BNBT6-*x*Sm ceramics at 20°–80°. (d) XRD patterns of 32°–33°. (e) The lattice parameters of porous BNBT6-*x*Sm ceramics.

Figure 1b shows the SEM images of porous BNBT6 ceramics with a 10 wt.% pollen addition, exhibiting a uniformly distributed ellipsoidal closed-pore structure. The inserted image depicts the microstructure of kiwifruit pollen, with a radial length of approximately 20  $\mu\text{m}$  and a lateral length of approximately 10  $\mu\text{m}$ . The pollen's shape closely resembles the porous structure, resulting from the gas escaping during the high-temperature sintering process, resulting in the same structure as the pollen template pores. In comparison to other biotemplate pore-forming agents, the lower density of pollen allows for the fabrication of high-porosity ceramics with ease.

The XRD diffractograms of the porous BNBT6- $x\text{Sm}$  ceramic powders are shown in Figure 1c. The addition of pollen as a pore-forming agent has no effect on the structure of BNBT6 ceramics. The peak positions of the prepared porous BNBT6- $x\text{Sm}$  ceramics correspond to the standard PDF#46-0001 card, showing a single-phase structure, and its strongest peak position between  $32^\circ$ – $33^\circ$  corresponds to the Miller index (110) in the standard card. This indicates that the synthesized sample shows a perovskite phase structure without secondary phases and that  $\text{Sm}^{3+}$  is doped into the lattice and forms a single-phase solid solution with BNBT6. Figure 1d shows the diffraction peaks from  $32^\circ$  to  $33^\circ$ , which shift to higher angles with an increase in doping amount. Upon comparing the ionic radii of  $\text{Sm}^{3+}$  with A and B site ions, it was discovered that  $\text{Sm}^{3+}$  is likely to substitute the A site because of its smaller ionic radius (0.0958 nm) when compared to  $\text{Na}^+$  (0.139 nm),  $\text{Bi}^{3+}$  (0.138 nm), and  $\text{Ba}^{2+}$  (0.161 nm). The XRD patterns of porous BNBT6- $x\text{Sm}$  ceramics were refined using jade. The lattice parameters (a, b, c) and cell volume (V) corresponding to different  $\text{Sm}^{3+}$  doping were calculated, as shown in Figure 1e. The lattice parameters (a, c) and cell volumes (V) decrease with the change in  $\text{Sm}^{3+}$  doping. An increase in the asymmetry of the lattice and the induction of lattice distortion occur. The lattice shrinkage results in a decrease in the lattice constant [31], signifying that  $\text{Sm}^{3+}$  has successfully entered the A-site of the porous BNBT6 ceramics.

Figure 2a–d depicts the SEM images of porous BNBT6- $x\text{Sm}$  ceramics, and Figure 2e–h shows the corresponding grain size distribution. Upon comparison, it was discovered that the average grain size is largest at  $x = 0.01$ , with grain refining occurring subsequently. This is attributed to the excessive  $\text{Sm}^{3+}$  concentration near the grain boundaries, which inhibits grain growth. The doped ceramics exhibit well-defined grain boundaries, uniform grain size, and strong bonding between grains, all of which can improve the mechanical strength of piezoelectric ceramics and be advantageous for piezoelectric ceramic applications [32,33]. It is noteworthy that doping does not affect the porosity and bulk density of porous ceramics, and the porosity of BNBT6- $x\text{Sm}$  ceramics measured using the Archimedes drainage method averaged about 28.7% for a pollen addition of 10 wt.% and a bulk density of about  $4.264 \text{ g/cm}^3$ .

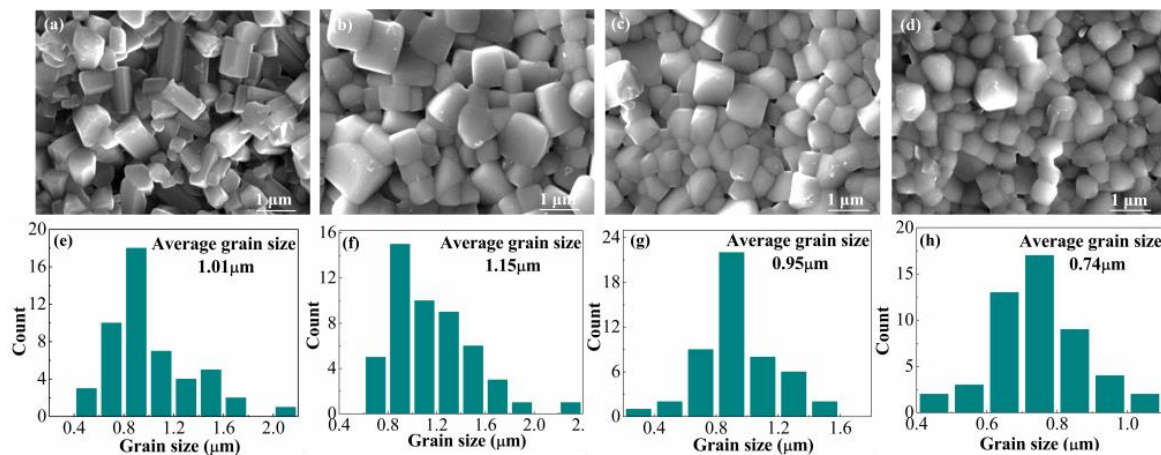


**Figure 2.** SEM images of surface and grain size distribution for porous BNBT6- $x\text{Sm}$  ceramics at (a,e)  $x = 0$ , (b,f)  $x = 0.01$ , (c,g)  $x = 0.02$ , and (d,h)  $x = 0.04$ .

### 3.2. Dielectric Properties of the Porous BNBT6-xSm Ceramics

Figure 3a–e shows the dielectric constant ( $\epsilon_r$ ) and dielectric loss ( $\tan\delta$ ) of porous BNBT6-xSm ceramics at various frequencies, ranging from room temperature to 450 °C. As can be seen from the figures, porous BNBT6-xSm ceramics exhibit two distinct peaks at around 150 °C and 300 °C, indicating different phase transition processes that occur within the tested temperature range [34]. The dielectric loss is higher at low frequency, which is attributed to the inhomogeneous charge distribution at the pore interface, as demonstrated by Maxwell–Wagner relaxation [35]. Figure 4a shows the dielectric constant versus temperature for porous BNBT6-Sm ceramics at 100 kHz. As can be seen from the figure, the sample with  $x = 0.01$  has a high relative permittivity ( $\epsilon_r = 782$ ) at room temperature. Compared to BNBT6 ceramics, the dielectric maximum is significantly higher at  $x = 0.01$ , 1567 for BNBT6 ceramics, and 2364 for BNBT6-0.01Sm. The increase in dielectric constant is due to the replacement of the low valence positive ion ( $\text{Na}^+$ ) with a high valence positive ion ( $\text{Sm}^{3+}$ ), which causes cationic vacancies in the porous ceramic sample and makes it easier for the domain walls to move under the action of electric fields or external forces, thus softening its properties. This results in a softening of the properties, which in turn manifests as an increase in the dielectric constant. However, the maximum value of the dielectric constant decreases gradually when too much  $\text{Sm}_2\text{O}_3$  is added ( $x > 0.01$ ). This may result from the higher degree of A-site disorder introduced by Sm substitution. Figure 4b shows the corresponding dielectric loss versus temperature variation, and there is a clear peak of dielectric loss ( $\tan\delta$ ) near 100 °C. This change occurs because the distortion of the crystal structure after depolarization is small, the electric domains turn easily, and the relaxation polarization loss is small. At around 300 °C, the trend of the dielectric loss peak with temperature is small and the curve is relatively flat.

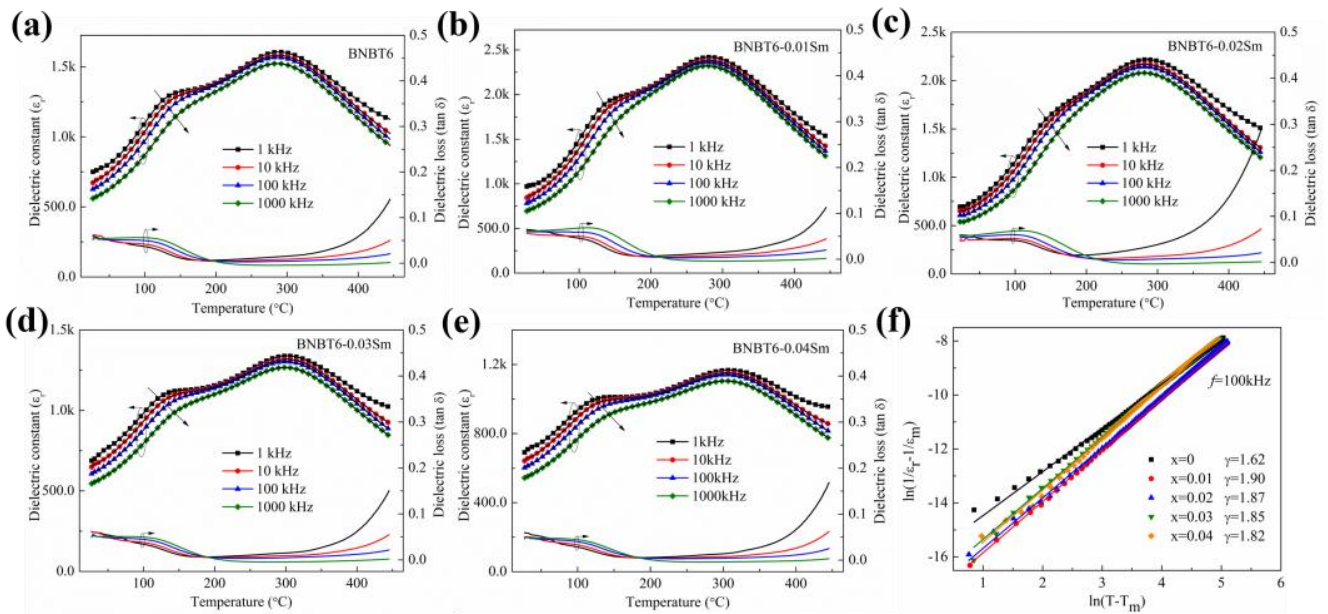


**Figure 3.** Temperature dependence of dielectric constant and dielectric loss of porous BNBT6-xSm ceramics at (a)  $x = 0$ , (b)  $x = 0.01$ , (c)  $x = 0.02$ , (d)  $x = 0.03$ , and (e)  $x = 0.04$ . (f) Plots of  $\ln(1/\epsilon_r - 1/\epsilon_m)$  as a function of  $\ln(T - T_m)$  for porous BNBT6-xSm ceramics at 100 kHz.

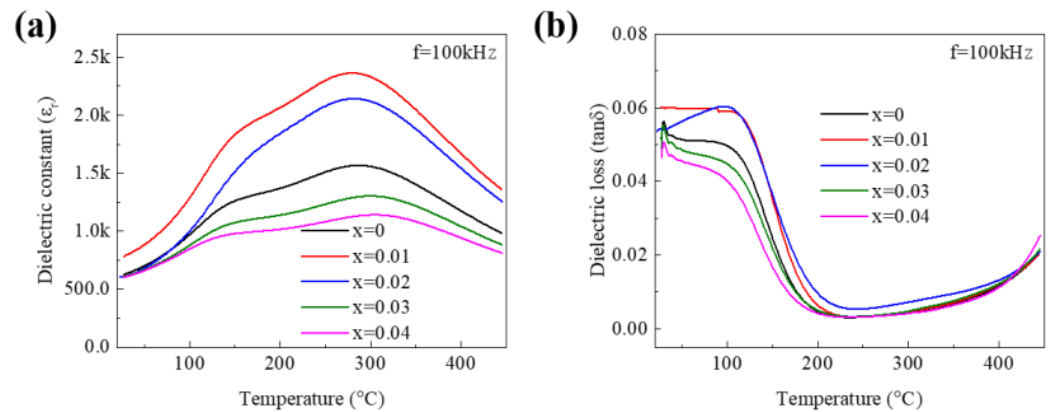


**Figure 4.** Temperature dependence of (a) dielectric constant, and (b) dielectric loss of porous BNBT6- $x$ Sm ceramics at 100 kHz.

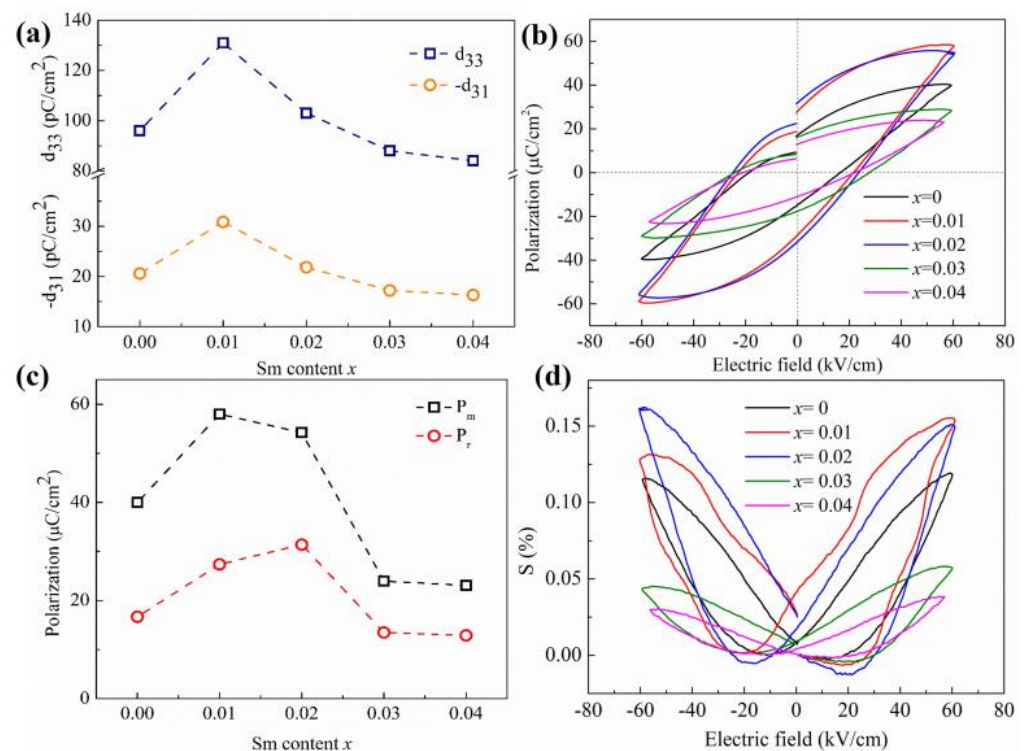
For different temperatures in the dielectric function diagram,  $T_m$  is the temperature corresponding to the maximum value of the dielectric constant, while  $T$  is the temperature corresponding to a point on the dielectric curve. When  $T < T_m$ , the porosity allows the air-pore interface to act as the pinning center for the domain wall under a non-uniform electric field, thus reducing domain wall motion and correlation loss. When  $T > T_m$ , the primary conductivity mechanism of porous BNBT6- $x$ Sm ceramics gradually changes from electronic conductivity to ionic conductivity, while the leakage current of the samples increases rapidly, leading to a rapid increase in the dielectric loss of porous BNBT6- $x$ Sm ceramics.

The plots of  $\ln(1/\epsilon_r - 1/\epsilon_m)$  as a function of  $\ln(T - T_m)$  for porous BNBT6- $x$ Sm ceramics at 100 kHz are presented in Figure 3f. The relaxor behavior of these ceramics can be analyzed using the modified Curie–Weiss law [36]. The addition of the pores increases the disorder in the direction of the long-range ordered dipole arrangement, and the pores act as pinning centers for domains on the wall of the pore. This results in hindered dipole turning and the relaxation of the depolarization process. The slope of the linear fit in the figure represents the relaxation factor  $\gamma$  of the porous BNBT6- $x$ Sm ceramic, which characterizes the parameter of relaxation dispersion. For porous BNBT6- $x$ Sm ceramics, the values of relaxation factor  $\gamma$  are greater than 1 and close to 2, indicating typical relaxor behavior. The maximum value of  $\gamma$  is found to be 1.90 at  $x = 0.01$ , indicating that the addition of  $\text{Sm}^{3+}$  further enhances the relaxor behavior in porous BNBT6- $x$ Sm ceramics. The presence of  $\text{Na}^+$ ,  $\text{Ba}^{2+}$ ,  $\text{Bi}^{3+}$ , and  $\text{Sm}^{3+}$  ions at the A-site in porous BNBT6- $x$ Sm ceramics causes inhomogeneity in the chemical composition and crystal structure at the nanoscale level. This inhomogeneity creates regions with higher concentrations of certain components, leading to relaxor ferroelectric behavior, as predicted by the constituent fluctuation theory. Porous BNBT6- $x$ Sm ceramics exhibit typical characteristics of relaxor ferroelectrics, such as wide dielectric peaks and frequency dispersion. In soft doping,  $\text{Sm}^{3+}$  acts as a donor ion, generating cation vacancies at the A-site. This leads to the suppression of the coupling between Ti-O bonds, enhancing the relaxor ferroelectric behaviors [37].

### 3.3. Piezoelectric and Ferroelectric Properties of the Porous BNBT6- $x$ Sm Ceramics

Figure 5a illustrates the longitudinal piezoelectric coefficients ( $d_{33}$ ) and transverse piezoelectric coefficients ( $-d_{31}$ ) of porous BNBT6- $x$ Sm ceramics. As the doping of  $\text{Sm}^{3+}$  increases, the piezoelectric coefficient exhibits an alternating trend, and both  $d_{33}$  and  $-d_{31}$  reach their maximum value at  $x = 0.01$ , with values of 131 pC/N and 30.88 pC/N, respectively. The introduction of  $\text{Sm}^{3+}$  soft doping in the porous structure results in cation vacancies in the A-site, making the domain wall motion easy. The different ionic radii of the dopant ions induce lattice distortion and facilitate domain switching. More domains are oriented along the electric field direction during polarization, so the piezoelectric properties are improved [37]. Doping introduces more ions into the BNBT6 lattice, which increases ionic activity and enhances the piezoelectric properties of the porous ceramics [38]. How-

ever, when more  $\text{Sm}^{3+}$  ions are added, lattice distortion increases and domain switching becomes more difficult [39], leading to a decrease in the piezoelectric properties.



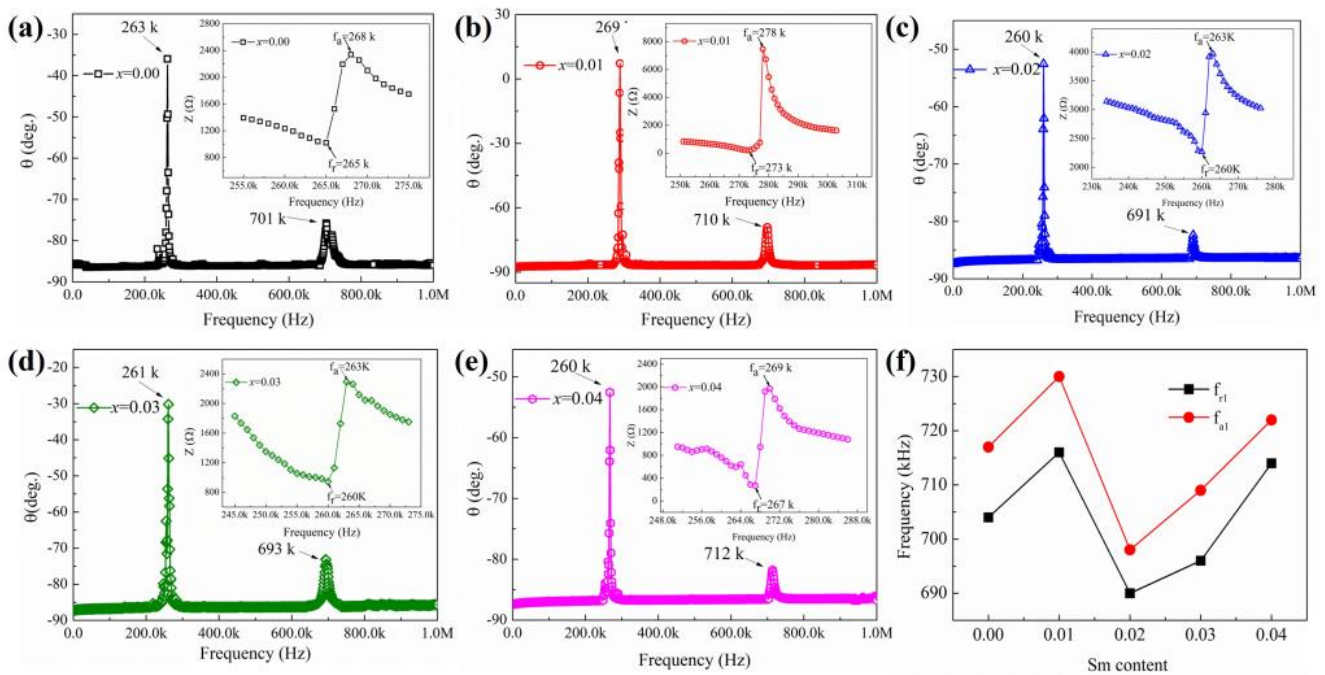
**Figure 5.** (a) Longitudinal piezoelectric coefficient ( $d_{33}$ ) and the transverse piezoelectric coefficient ( $-d_{31}$ ) of porous BNBT6- $x$ Sm ceramics. (b) Hysteresis loops of porous BNBT6- $x$ Sm ceramics. (c) Polarization including  $P_m$  and  $P_r$ . (d) Strain–electric loops of porous BNBT6- $x$ Sm ceramics at 60 kV/cm.

Figure 5b depicts the hysteresis loops of porous BNBT6- $x$ Sm ceramics under the electric field of 60 kV/cm, which shows the typical hysteresis loops characteristics of relaxor ferroelectrics. The polarization intensities at room temperature show a trend of first increasing and then decreasing under the same electric field strength. This trend is more clearly shown in Figure 5c, which displays the polarization intensities  $P_m$  and  $P_r$ . For the same system, the piezoelectric properties are better when the remanent polarization  $P_r$  is higher [40]. However, when the doping amount of  $\text{Sm}^{3+}$  exceeds 0.01, the  $d_{33}$  gradually decreases, indicating that excess  $\text{Sm}^{3+}$  doping does not necessarily increase the  $d_{33}$  of porous BNBT6 ceramics. This is because the long-range ferroelectric domains are destroyed when the doping concentration reaches a certain level, leading to an increase in the difficulty of polarization. Consequently, the polarization intensities decrease and the piezoelectric properties are weakened.

Figure 5d depicts the strain–electric loops (S-E loops) of porous BNBT6- $x$ Sm ceramics under the effect of 60 kV/cm alternating electric field. The S-E loops exhibit a standard “butterfly shape” with both positive and negative strains, indicating typical ferroelectric characteristics. The positive strain of undoped porous BNBT6 ceramic is 0.118%. With the introduction of  $\text{Sm}^{3+}$  doping into the porous BNBT6 ceramic system, the positive strain initially increases and then decreases, with a maximum positive strain of 0.154% observed at  $x = 0.01$ . Furthermore, the negative strain almost disappears when  $x = 0.04$ . These phenomena suggest that increasing the amount of  $\text{Sm}^{3+}$  doping components to a certain extent results in a decrease in the long-range ferroelectric phase and an increase in the relaxation phase in the system.

### 3.4. Piezoelectric Resonance Characteristics of the Porous BNBT6-*x*Sm Ceramics

Figure 6a–e shows the impedance angle spectrum of the porous BNBT6-*x*Sm ceramics in the radial extension vibration mode and the impedance spectrum under fundamental frequency. In order to avoid vibration coupling interference, the thickness (*h*) of the oscillator should be much smaller than the diameter (*d*). The porous BNBT6-*x*Sm ceramics samples are designed with thickness *h* = 0.6 mm and diameter *d* = 13.2~14.1 mm to create a radial extension vibration. The impedance angle spectrum of all samples shows only two resonance peaks within the range of 0 to 1 MHz, which corresponds to the first-order resonance frequency (fundamental frequency) and the second-order resonance frequency (first harmonic frequency) of the radial extension vibration.



**Figure 6.** Impedance angle spectrum and impedance spectrum under fundamental frequency of porous BNBT6-*x*Sm ceramics at (a) *x* = 0, (b) *x* = 0.01, (c) *x* = 0.02, (d) *x* = 0.03, and (e) *x* = 0.04. (f) Resonant frequency ( $f_{r1}$ ) and anti-resonant frequency ( $f_{a1}$ ) under the first harmonic frequency of porous BNBT6-*x*Sm ceramics.

The inset images in Figure 6a–e show the impedance spectrum under the fundamental frequency for porous BNBT6-*x*Sm ceramics, which exhibit the characteristic coupling “N-shaped peak”. In the figure,  $f_r$  and  $f_a$  denote the resonant frequency and anti-resonant frequency, respectively. The figure indicates that the main peak (maximum  $\theta$ ) is significantly higher than other resonant peaks in this mode, and the resonant fundamental frequency is low, making it difficult to induce resonant coupling. Furthermore, the diameter of the sample size is much larger than the thickness, allowing for a larger gas adsorption area with the same thickness, while also having a shorter polarization distance for the piezoelectric oscillator, making excitation easier.

Figure 6f shows the resonant frequency  $f_{r1}$  and the anti-resonant frequency  $f_{a1}$  of the porous BNBT6-*x*Sm ceramics under the first harmonic frequency. The resonant frequency shows an undulating trend with increased  $\text{Sm}^{3+}$  doping. Additionally, the change in  $\text{Sm}^{3+}$  doping corresponds to different resonant frequencies, with both  $f_{r1}$  and  $f_{a1}$  reaching a maximum at *x* = 0.01.

Based on the data presented above, the values of  $f_r$ ,  $f_a$ ,  $f_{r1}$ , and  $f_{a1}$  can be obtained, and then the plane electromechanical coupling coefficient ( $k_p$ ), Poisson’s ratio ( $\sigma$ ), elastic compliance coefficient ( $S_{11}^E$ ), transverse electromechanical coupling coefficient ( $k_{31}$ ), and transverse piezoelectric constant ( $-d_{31}$ ) of the samples can be calculated.

According to the following formulas:  
the plane electromechanical coupling coefficient ( $k_p$ ):

$$\frac{1}{k_p^2} = 0.395 \frac{f_r}{\Delta f} + 0.574 = 0.395 \frac{f_r}{f_a - f_r} \tag{1}$$

Poisson’s ratio ( $\sigma$ ):

$$\sigma = \frac{5.332f_r - 1.867f_{r1}}{0.6054f_{r1} - 0.1910f_r} \tag{2}$$

when the first-order approximation is taken:

$$\eta_1 = 1.867 + 0.604\sigma \tag{3}$$

elastic compliance coefficient ( $S_{11}^E$ ):

$$S_{11}^E = \frac{\eta_1^2}{\pi^2 d^2 \rho_b (1 - \sigma^2) f_r^2} \tag{4}$$

transverse electromechanical coupling coefficient ( $k_{31}$ ):

$$k_{31} = \left( \frac{2}{1 - \sigma} \right)^{-\frac{1}{2}} k_p \tag{5}$$

transverse piezoelectric constant ( $-d_{31}$ ):

$$-d_{31} = k_{31} \sqrt{\epsilon_{33}^T S_{11}^E} \tag{6}$$

Formula:  $\rho_b$ —is the density of porous piezoelectric ceramics ( $4264 \text{ kg/m}^3$ ) and  $d$  is the diameter of the thin wafer sample.

Figure 7a presents the variation of electromechanical coupling parameters of porous BNBT6- $x$ Sm ceramics, and the main parameters are shown in Table 1. It can be observed that the values of  $k_p$ ,  $\sigma$ ,  $S_{11}^E$ ,  $k_{31}$ , and  $-d_{31}$  of the  $\text{Sm}^{3+}$  doping porous BNBT6 ceramics are changed when compared to the porous BNBT6- $x$ Sm ceramics. When  $x = 0.01$ ,  $k_p = 0.213$ ,  $\sigma = 0.31$ ,  $S_{11}^E = 8.85 \text{ pN/m}^2$ ,  $k_{31} = 0.125$ , and  $-d_{31} = 30.88 \text{ pC/N}$ .

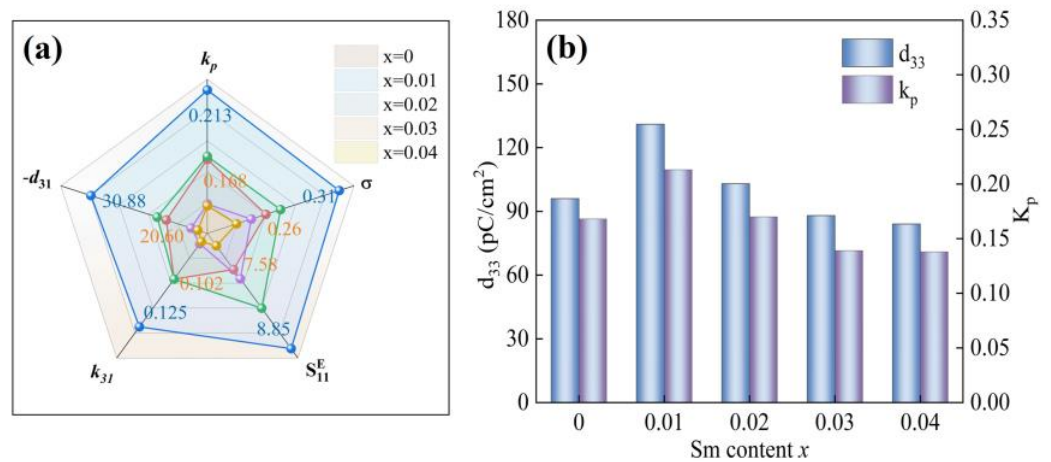


**Figure 7.** (a) Electromechanical coupling parameters of porous BNBT6- $x$ Sm ceramics. (b) Variation  $d_{33}$  and  $k_p$  of porous BNBT6- $x$ Sm ceramics with  $x$ .

**Table 1.** Electromechanical coupling parameters of porous BNBT6-*x*Sm ceramics.

Samples	$k_p$	$\sigma$	$\eta_1$	$S_{11}^E$ (pN/m <sup>2</sup> )	$k_{31}$	$-d_{31}$ (pC/N)
$x = 0$	0.168	0.26	2.02	7.58	0.102	20.60
$x = 0.01$	0.213	0.31	2.05	8.85	0.125	30.88
$x = 0.02$	0.170	0.27	2.03	8.20	0.102	21.83
$x = 0.03$	0.139	0.25	2.01	7.73	0.085	17.21
$x = 0.04$	0.1379	0.24	2.01	7.20	0.084	16.30

Figure 7b illustrates those changes in Sm<sup>3+</sup> doping affect both the plane electromechanical coupling coefficients and the piezoelectric coefficients similarly. The modified Sm<sup>3+</sup> donor-type has an impact on  $k_p$  and  $d_{33}$ , which are influenced by domain wall mobility [41]. The improved motion of domain walls leads to increased values of  $d_{33}$  and  $k_p$ . The performance parameters of porous BNBT6-0.01Sm ceramics are relatively superior compared to the properties of PZT-8 ceramics utilized in practical applications. Specifically, the  $-d_{31}$  is 33.2% of that of PZT-8 (93), the  $k_p$  is 42.5% of that of PZT-8 (0.5), and the  $S_{11}^E$  is 77.5% of that of PZT-8 (11.1). These superior performance parameters make it a promising candidate for use in piezoelectric resonant gas sensors.

#### 4. Conclusions

In this study, the porous (Bi<sub>0.5</sub>Na<sub>0.5</sub>)<sub>0.94</sub>Ba<sub>0.06</sub>TiO<sub>3</sub> ceramics with a pollen addition of 10 wt.% were modulated through Sm<sup>3+</sup> doping. The effects of Sm<sup>3+</sup> doping on dielectric, piezoelectric, and resonance characteristics of the porous BNBT6 ceramics were analyzed. The results indicated that the ceramic grain size initially increased with doping but were then refined continuously. The introduction of pores caused relaxation of the depolarization process, and soft Sm<sup>3+</sup> doping enhanced relaxor ferroelectric behavior. The doping of Sm<sup>3+</sup> as donor ion induced lattice distortion and generated cation vacancies at the A-site, which facilitates domain wall motion and domain switching under the action of an external electric field. These changes significantly improved piezoelectric properties and the electromechanical coupling parameters of the ceramics. At  $x = 0.01$ , it was found that  $d_{33} = 131$  pC/N,  $k_p = 0.213$ , and  $S_{11}^E = 8.85$  pN/m<sup>2</sup>,  $k_{31} = 0.125$ . Doping under the porous structure increased the resonant frequency and improved the piezoelectric resonance characteristics. Therefore, porous BNBT6 ceramics with appropriately doped Sm<sup>3+</sup> are viable substrate materials for high-sensitivity piezoelectric resonators. The combined modification of pores and ions also provides a new approach for optimizing the performance of piezoelectric materials based on structural optimization.

**Author Contributions:** S.X.: methodology; writing—original draft. H.D.: conceptualization. Z.L.: formal analysis; data curation. F.Z.: investigation; visualization. Q.L.: writing—review and editing. Y.H.: validation. L.K.: resources. All authors have read and agreed to the published version of the manuscript.

**Funding:** Funding was provided by the National Natural Science Foundation of China (52172099) and Provincial Joint Fund of Shaanxi (2021JLM-28).

**Institutional Review Board Statement:** Not applicable.

**Informed Consent Statement:** Not applicable.

**Data Availability Statement:** Data will be made available on request.

**Acknowledgments:** This work was supported by the National Natural Science Foundation of China under grant number 52172099 and the Provincial Joint Fund of Shaanxi under grant number 2021JLM-28.

**Conflicts of Interest:** The authors declare that they have no known competing financial interests or personal relationships that could have appeared to influence the work reported in this paper.

## References

1. Martinez, T.; Pillonnet, G.; Loyau, V.; Vasic, D.; Costa, F. A transverse traveling wave piezoelectric transformer. *Smart Mater. Struct.* **2019**, *28*, 16. [\[CrossRef\]](#)
2. Ran, H.P.; Du, H.L.; Ma, C.Y.; Zhao, Y.Y.; Feng, D.N.; Xu, H. Effects of A/B-Site Co-Doping on Microstructure and Dielectric Thermal Stability of AgNbO<sub>3</sub> Ceramics. *Sci. Adv. Mater.* **2021**, *13*, 741–747. [\[CrossRef\]](#)
3. Du, H.L.; Ma, C.Y.; Ma, W.X.; Wang, H.T. Microstructure evolution and dielectric properties of Ce-doped SrBi<sub>4</sub>Ti<sub>4</sub>O<sub>15</sub> ceramics synthesized via glycine-nitrate process. *Process. Appl. Ceram.* **2018**, *12*, 303–312. [\[CrossRef\]](#)
4. Anastasia, K.; Marina, D.; Nellya, P.; Liana, P.; Alexandr, F. Preparation and dielectric properties of thermo-vaporous barium titanate ceramics. *Mater. Technol.* **2015**, *3*, 447–451. [\[CrossRef\]](#)
5. Rodel, J.; Webber, K.G.; Dittmer, R.; Jo, W.; Kimura, M.; Damjanovic, D. Transferring lead-free piezoelectric ceramics into application. *J. Eur. Ceram. Soc.* **2015**, *35*, 1659–1681. [\[CrossRef\]](#)
6. Feng, D.N.; Du, H.L.; Ran, H.P.; Lu, T.; Xia, S.Y.; Xu, L.; Wang, Z.X.; Ma, C.Y. Antiferroelectric stability and energy storage properties of Co-doped AgNbO<sub>3</sub> ceramics. *J. Solid State Chem.* **2022**, *310*, 7. [\[CrossRef\]](#)
7. Ma, C.Y.; Du, H.L.; Liu, J.; Kang, L.; Du, X.; Xi, X.Y.; Ran, H.P. High-temperature stability of dielectric and energy-storage properties of weakly-coupled relaxor (1 – x)BaTiO<sub>3</sub>-xBi(Y<sub>1/3</sub>Ti<sub>1/2</sub>)O<sub>3</sub> ceramics. *Ceram. Int.* **2021**, *47*, 25029–25036. [\[CrossRef\]](#)
8. Dittmer, R.; Jo, W.; Rdel, J.; Kalinin, S.; Balke, N. Nanoscale Insight Into Lead-Free BNT-BT-xKNN. *Adv. Funct. Mater.* **2012**, *22*, 4208–4215. [\[CrossRef\]](#)
9. Zhang, S.T.; Kouniga, A.B.; Aulbach, E.; Ehrenberg, H.; Rdel, J. Giant strain in lead-free piezoceramics Bi<sub>0.5</sub>Na<sub>0.5</sub>TiO<sub>3</sub>-BaTiO<sub>3</sub>-K<sub>0.5</sub>Na<sub>0.5</sub>NbO<sub>3</sub> system. *Appl. Phys. Lett.* **2007**, *91*, 112906. [\[CrossRef\]](#)
10. Zhang, H.Z.; Zhu, M.K.; Hou, Y.D.; Wang, R.Z.; Yan, H.; Liu, L.Y. Structural Modulation of Na<sub>0.5</sub>Bi<sub>0.5</sub>TiO<sub>3</sub> in Hydrothermal Synthesis. *Int. J. Appl. Ceram. Technol.* **2016**, *13*, 569–578. [\[CrossRef\]](#)
11. Zhang, M.; Wang, W.; Xia, G.; Wang, L.; Wang, K. Self-Powered Electronic Skin for Remote Human–Machine Synchronization. *ACS Appl. Electron. Mater.* **2023**, *5*, 498–508. [\[CrossRef\]](#)
12. Xu, C.; Lin, D.; Kwok, K.W. Structure, electrical properties and depolarization temperature of (Bi<sub>0.5</sub>Na<sub>0.5</sub>)TiO<sub>3</sub>-BaTiO<sub>3</sub> lead-free piezoelectric ceramics. *Solid State Sci.* **2008**, *10*, 934–940. [\[CrossRef\]](#)
13. Liu, G.; Button, T.W.; Zhang, D. Lamellar BaTiO<sub>3</sub> and its composites fabricated by the freeze casting technique. *J. Eur. Ceram. Soc.* **2014**, *34*, 4083–4088. [\[CrossRef\]](#)
14. Polley, C.; Distler, T.; Detsch, R.; Lund, H.; Springer, A.; Boccaccini, A.R.; Seitz, H. 3D Printing of Piezoelectric Barium Titanate-Hydroxyapatite Scaffolds with Interconnected Porosity for Bone Tissue Engineering. *Materials* **2020**, *13*, 1773. [\[CrossRef\]](#)
15. Park, K.; Kim, Y.S.; Jo, S.; Lee, Y.W. Polarization-Interference-Based Fiber Vibration Sensor Incorporating Polarization-Diversity Loop Structure. *IEEE Sens. J.* **2016**, *16*, 1949–1955. [\[CrossRef\]](#)
16. Takenaka, T.; Maruyama, K.; Sakata, K. (Bi<sub>1/2</sub>Na<sub>1/2</sub>)TiO<sub>3</sub>-BaTiO<sub>3</sub> System for Lead-Free Piezoelectric Ceramics. *Jpn. J. Appl. Phys.* **1991**, *30*, 2236–2239. [\[CrossRef\]](#)
17. He, Z.; Shi, S.; Pan, Z.; Tang, L.; Zhao, J.; Shen, Y.; Hu, D.; Chen, Y.; Li, P.; Liu, J.; et al. Low Electric Field induced High Energy Storage Capability of the Free-lead Relaxor Ferroelectric 0.94Bi<sub>0.5</sub>Na<sub>0.5</sub>TiO<sub>3</sub>-0.06BaTiO<sub>3</sub>-based Ceramics. *Ceram. Int.* **2021**, *47*, 11611–11617.
18. Acosta, M.; Novak, N.; Rojas, V.; Patel, S.; Vaish, R.; Koruza, J.; Rossetti, G.A.; Rodel, J. BaTiO<sub>3</sub>-based piezoelectrics: Fundamentals, current status, and perspectives. *Appl. Phys. Rev.* **2017**, *4*, 53. [\[CrossRef\]](#)
19. Giannakoudakis, D.A.; Barczak, M.; Pearsall, F.; O'Brien, S.; Bandosz, T.J. Composite porous carbon textile with deposited barium titanate nanospheres as wearable protection medium against toxic vapors. *Chem. Eng. J.* **2020**, *384*, 9. [\[CrossRef\]](#)
20. Zhang, M.; Liu, Y.; Li, D.; Cui, X.; Wang, L.; Li, L.; Wang, K. Electrochemical Impedance Spectroscopy: A New Chapter in the Fast and Accurate Estimation of the State of Health for Lithium-Ion Batteries. *Energies* **2023**, *16*, 1599. [\[CrossRef\]](#)
21. Liu, W.; Cao, Y.; Wang, J.H.; Wang, Y.Z.; Xi, X.Q.; Yang, J.L. Piezoelectric properties of 3-1 type porous PMN-PZT ceramics doped with strontium. *Mater. Sci. Eng. B* **2021**, *263*, 5. [\[CrossRef\]](#)
22. Xu, T.T.; Wang, C.A. Control of pore size and wall thickness of 3-1 type porous PZT ceramics during freeze-casting process. *Mater. Des.* **2016**, *91*, 242–247. [\[CrossRef\]](#)
23. Yan, M.Y.; Xiao, Z.D.; Ye, J.J.; Yuan, X.; Li, Z.H.; Bowen, C.; Zhang, Y.; Zhang, D. Porous ferroelectric materials for energy technologies: Current status and future perspectives. *Energy Environ. Sci.* **2021**, *14*, 6158–6190. [\[CrossRef\]](#)
24. Liu, H.; Lin, X.J.; Zhang, S.; Huan, Y.; Huang, S.F.; Cheng, X. Enhanced performance of piezoelectric composite nanogenerator based on gradient porous PZT ceramic structure for energy harvesting. *J. Mater. Chem. A* **2020**, *8*, 19631–19640. [\[CrossRef\]](#)
25. Yap, E.W.; Glaum, J.; Oddershede, J.; Daniels, J.E. Effect of porosity on the ferroelectric and piezoelectric properties of (Ba<sub>0.85</sub>Ca<sub>0.15</sub>)(Zr<sub>0.1</sub>Ti<sub>0.9</sub>)O<sub>3</sub> piezoelectric ceramics. *Scr. Mater.* **2018**, *145*, 122–125. [\[CrossRef\]](#)
26. Wu, L.; Shi, X.; Du, H.L.; An, Q.L.; Li, Z.; Xu, H.; Ran, H.P. Ce-doped LaCoO<sub>3</sub> film as a promising gas sensor for ethanol. *AIP Adv.* **2021**, *11*, 8. [\[CrossRef\]](#)
27. Fan, P.Y.; Liu, K.; Ma, W.G.; Tan, H.; Zhang, Q.; Zhang, L.; Zhou, C.R.; Salamon, D.; Zhang, S.T.; Zhang, Y.J.; et al. Progress and perspective of high strain NBT-based lead-free piezoceramics and multilayer actuators. *J. Mater.* **2021**, *7*, 508–544. [\[CrossRef\]](#)
28. Hao, J.G.; Xu, Z.J.; Chu, R.Q.; Li, W.; Fu, P.; Du, J.; Li, G.R. Large electrostrictive effect and strong photoluminescence in rare-earth modified lead-free (Bi<sub>0.5</sub>Na<sub>0.5</sub>)TiO<sub>3</sub>-based piezoelectric ceramics. *Scr. Mater.* **2016**, *122*, 10–13. [\[CrossRef\]](#)

29. Kong, Y.X.; Zhao, H.Y.; Li, L.T.; Long, Y.; Hao, J.G. Effects of oxide additives on the electrical properties of sodium bismuth titanate-based lead-free ceramics. *Mater. Res. Bull.* **2020**, *122*, 5. [[CrossRef](#)]
30. Fu, P.; Xu, Z.; Chu, R.; Li, W.; Zang, G.; Hao, J. Piezoelectric, ferroelectric and dielectric properties of Sm<sub>2</sub>O<sub>3</sub>-doped (Bi<sub>0.5</sub>Na<sub>0.5</sub>)<sub>0.94</sub>Ba<sub>0.06</sub>TiO<sub>3</sub> lead-free ceramics. *Mater. Chem. Phys.* **2010**, *124*, 1065–1070. [[CrossRef](#)]
31. Ma, X.; Yin, J.T.; Zhou, Q.L.; Xue, L.H.; Yan, Y.W. Effect of Eu doping on structure and electrical properties of lead-free (Bi<sub>0.5</sub>Na<sub>0.5</sub>)(0.94)Ba<sub>0.06</sub>TiO<sub>3</sub> ceramics. *Ceram. Int.* **2014**, *40*, 7007–7013. [[CrossRef](#)]
32. Yao, Z.; Liu, H.; Liu, Y.; Wu, Z.; Shen, Z.; Liu, Y.; Cao, M. Structure and dielectric behavior of Nd-doped BaTiO<sub>3</sub> perovskites. *Mater. Chem. Phys.* **2008**, *109*, 475–481. [[CrossRef](#)]
33. Bian, S.S.; Yue, Z.X.; Zhang, J.; Li, L.T. Enhancement of dielectric properties and energy storage performance in 3Y-TZP ceramics with BaTiO<sub>3</sub> additives. *Int. J. Appl. Ceram. Technol.* **2020**, *17*, 1362–1370. [[CrossRef](#)]
34. Li, H. Some effects of different additives on dielectric and piezoelectric properties of (Bi<sub>1/2</sub>Na<sub>1/2</sub>)TiO<sub>3</sub>-BaTiO<sub>3</sub> morphotropic-phase-boundary composition. *Mater. Lett.* **2004**, *58*, 1194–1198. [[CrossRef](#)]
35. Lukacs, V.A.; Stanculescu, R.; Curecheriu, L.; Ciomaga, C.E.; Horchidan, N.; Cioclea, C.; Mitoseriu, L. Structural and functional properties of BaTiO<sub>3</sub> porous ceramics produced by using pollen as sacrificial template. *Ceram. Int.* **2020**, *46*, 523–530. [[CrossRef](#)]
36. Yuan, Q.B.; Li, G.; Yao, F.Z.; Cheng, S.D.; Wang, Y.F.; Ma, R.; Mi, S.B.; Gu, M.; Wang, K.; Li, J.F.; et al. Simultaneously achieved temperature-insensitive high energy density and efficiency in domain engineered BaTiO<sub>3</sub>-Bi(Mg<sub>0.5</sub>Zr<sub>0.5</sub>)O<sub>3</sub> lead-free relaxor ferroelectrics. *Nano Energy* **2018**, *52*, 203–210. [[CrossRef](#)]
37. Arshad, M.; Du, H.L.; Javed, M.S.; Maqsood, A.; Ashraf, I.; Hussain, S.; Ma, W.L.; Ran, H.P. Fabrication, structure, and frequency-dependent electrical and dielectric properties of Sr-doped BaTiO<sub>3</sub> ceramics. *Ceram. Int.* **2020**, *46*, 2238–2246. [[CrossRef](#)]
38. Kang, W.; Zheng, Z.; Li, Y.; Zhao, R.; Dun, W.; Wang, Y. Effect of doping Gd<sub>2</sub>O<sub>3</sub> on dielectric and piezoelectric properties of BaZr<sub>0.1</sub>Ti<sub>0.9</sub>O<sub>3</sub> ceramics by sol-gel method. *J. Mater. Sci.* **2019**, *30*, 2743–2749. [[CrossRef](#)]
39. Choudhury, S.; Li, Y.L.; Chen, L.Q.; Jia, Q.X. Strain Effect on Coercive Field of Epitaxial Barium Titanate Thin Films. *Appl. Phys. Lett.* **2008**, *92*, 142907. [[CrossRef](#)]
40. Wada, T.; Toyoiike, K.; Imanaka, Y.; Matsuo, Y. Dielectric and Piezoelectric Properties of (A<sub>0.5</sub>Bi<sub>0.5</sub>)TiO<sub>3</sub>-ANbO<sub>3</sub>(A=Na, K) Systems. *Jpn. J. Appl. Phys.* **2001**, *40*, 5703. [[CrossRef](#)]
41. Jaiban, P.; Namsar, O.; Jiansirisomboon, S.; Watcharapasorn, A.; Yimnirun, R. Electrical Properties of La-Doped Ba<sub>0.7</sub>Ca<sub>0.3</sub>TiO<sub>3</sub> Lead-Free Ceramics. *Ferroelectrics* **2015**, *487*, 86–93. [[CrossRef](#)]

**Disclaimer/Publisher's Note:** The statements, opinions and data contained in all publications are solely those of the individual author(s) and contributor(s) and not of MDPI and/or the editor(s). MDPI and/or the editor(s) disclaim responsibility for any injury to people or property resulting from any ideas, methods, instructions or products referred to in the content.